TITLE:

Decoding the olfactory map: targeted transcriptomics link olfactory sensory neurons to glomeruli

AUTHORS:

Kevin W. Zhu[1], Shawn D. Burton[2,3], Maira H. Nagai[1], Justin D. Silverman[4,5,6,7], Claire A. de March[1], Matt Wachowiak[3,*], Hiroaki Matsunami[1,8,9,*]

AFFILIATIONS:

[1]Department of Molecular Genetics and Microbiology, Duke University Medical Center; Durham, North Carolina, 27710, USA

[2]Department of Biological Sciences, Lehigh University; Bethlehem, Pennsylvania, 18015, USA

[3]Department of Neurobiology, University of Utah School of Medicine; Salt Lake City, Utah, 84112, USA

[4]College of Information Science and Technology, Pennsylvania State University; University Park, Pennsylvania, 16802, USA

[5]Department of Statistics, Pennsylvania State University; University Park, Pennsylvania, 16802, USA

[6]Department of Medicine, Pennsylvania State University; Hershey, Pennsylvania, 17033, USA

[7]Institute for Computational and Data Science, Pennsylvania State University; University Park, 16802, USA

[8]Department of Neurobiology, Duke University Medical Center; Durham, North Carolina, 27710, USA

[9]Duke Institute for Brain Sciences, Duke University; Durham, North Carolina, 27710, USA

*Corresponding authors. Email: hiroaki.matsunami@duke.edu, matt.wachowiak@utah.edu

ONE SENTENCE SUMMARY:

Targeted enrichment of olfactory receptor mRNA in olfactory bulb sections determines spatial positions for murine glomeruli.

ABSTRACT:

Sensory processing in vertebrate olfactory systems is organized across olfactory bulb glomeruli, wherein axons of peripheral sensory neurons expressing the same olfactory receptor co-terminate to transmit receptor-specific activity to central neurons. Understanding how receptors map to glomeruli is therefore critical to understanding olfaction. High-throughput spatial transcriptomics is a rapidly advancing field, but low-abundance olfactory receptor expression within glomeruli has previously precluded high-throughput mapping of receptors to glomeruli. Here we combined spatial sectioning along the anteroposterior, dorsoventral, and mediolateral axes with target capture enrichment sequencing to overcome low-abundance target expression. This strategy allowed us to spatially map 86% of olfactory receptors across the olfactory bulb and uncover a relationship between OR sequence and glomerular position.

MAIN TEXT:

The organization of axonal projections from olfactory sensory neurons (OSNs) in the olfactory epithelium (OE) to glomeruli on the olfactory bulb (OB) forms the mammalian olfactory map (*1–4*). In the mouse, each canonical OSN expresses a single olfactory receptor (OR) or trace amine-associated receptor (TAAR) allele from a repertoire of over 1000 OR and TAAR genes. Insights into the organization of the olfactory map were first obtained using in

situ hybridization, where OR transcript probes indicated the convergence of OSN axons into discrete structures called glomeruli on the OB surface, which range from 50 to 120 μm in diameter (*3*, *5*, *6*). Later, this organization was more clearly visualized through the use of gene-targeted mouse lines, which demonstrated that glomeruli are formed from the axonal convergence of OSNs expressing the same OR gene (*7*). Together these studies established the convergence of homotypic OSN axons to stereotyped glomeruli whose positional variability ranges from 75 to 270 μm depending on OR identity (*5*, *8*). Because each glomerulus represents a single OR and a single odorant can bind multiple ORs, odor signals detected in the OE are transformed into a map of glomerular activity on the OB (*9*–*13*).

To date, glomerular positions for only ~3% of mouse ORs are available, and further progress has been stymied due to the low-throughput, laborious, and time-consuming aspects of currently available methodologies for mapping each OR in the expansive murine repertoire (*7*, *8*, *13*–*29*). Furthermore, the ability to compare locations between multiple glomeruli is limited among these studies due to the lack of reference landmarks on the OB and differences between methodologies. A more efficient approach for mapping OR axon projections to OB glomeruli would serve to generate a more comprehensive and informative map that would serve as a foundation for further functional studies of odor coding and processing. In this study, we demonstrate that target capture enrichment on spatial samples from the OB enables detection of low-abundance OR and TAAR mRNA in the axon termini of OSNs. Using this approach, we map 86% of the 1118 ORs and TAARs along the anteroposterior, mediolateral, and dorsoventral axes and combine these data to generate a three-dimensional model of glomerular positions with a precision of 141 μm. We examine the relationship between OR sequence and OB position, identify the set of ORs and TAARs expressed within dorsal glomeruli accessible to functional imaging, and generate gene-

targeted mouse lines for two dorsal glomerular ORs amenable to functional characterization in vivo.

RESULTS

Targeted capture consistently enriches OR transcripts

Previous studies have detected low levels of OR mRNA in OSN axon terminals, identifying the glomerular positions for specific ORs within histological sections (*5*, *23*, *27*). To quantify OR and TAAR transcripts in the OB we first performed conventional RNA-Seq on whole-OB tissue from a mouse at postnatal day 21, an age when olfactory glomeruli are fully developed and finalized in their stereotyped positions (*30*, *31*). Quantification of 25.7 million reads identified 410/1118 (36.7%) intact ORs at an average abundance of 0.06 transcripts per million (TPM) (median OR TPM = 0, 6/15 (40%) TAARs with TPM above 0, mean TAAR TPM = 0.077, median TAAR TPM = 0) (Fig. 1, B and C), confirming the low abundance of OR mRNA in OSN axon terminals.

To enrich sampling for OR transcripts, we designed a target capture array against chemosensory receptor gene families primarily targeting ORs and TAARs (*32*). We applied this target capture array to the previously sequenced OB library and identified 842 of the 1118 ORs (75.3%) and 10 of the 15 TAARs (66.7%) (Fig. 1, A to C). Following targeted capture, these ORs were present in a set of 27.7 million reads at an average abundance of 360.27 TPM (median = 106.74 TPM, mean TAAR TPM = 871.66, median TAAR TPM = 64.62) resulting in a mean fold enrichment of 6005X (mean TAAR fold enrichment = 11320X) (Fig. 1, B and C). Spearman's rho for OR and TAAR transcript abundances between uncaptured and captured samples was 0.71 ($P < 2.2 \times 10^{-16}$). Further, four sets of independently captured technical replicates from two different OBs (two distinct spike-in mRNAs for RNA subsamples from each of the two bulbs, and two technical replicates per subsample) exhibited a

Spearman's rho of 0.95 ($P < 2.2 \times 10^{-16}$) (Fig. 1D and fig. S1D). The fold enrichment and correlation between pre- and post-capture samples indicates the targeted capture approach enriches the majority of ORs and TAARs in a highly consistent fashion as evidenced by the technical replicate correlation. The mean pairwise Spearman's rho for three biological replicate OBs was 0.83 ($P < 2.2 \times 10^{-16}$), indicating the relative abundance of OR and TAAR transcripts is conserved between individual animals (Fig. 1E and fig. S1E).

In summary, targeted capture consistently enriched OR and TAAR transcripts to levels that facilitate positional analysis. This encouraged us to conduct targeted capture of ORs and TAARs from sections of OB to determine which ORs were expressed in each section. We sectioned from three directions, dorsoventral (DV), anteroposterior (AP), and mediolateral (ML). We note that these three axes are not precisely orthogonal and not perfectly concordant with the corresponding reference features such as DV zonal boundaries and medial surface of the OB.

Expression of ORs and TAARs in dorsoventral OB sections correlates with OE expression zones

Pioneering investigation established that ORs are expressed in overlapping, continuous zones of the OE along the DV axis (*33*, *34*). This zonal OE organization further correlates with DV glomerular positions of OR expression in the OB (*7*, *23*, *35*), with more recent studies leveraging multiplexed assays and transcriptomics to map an expanded number of ORs to more specific OE zones (*36*, *37*). To comprehensively assess the relationship of OE-OB DV zonal organization of OR expression, we collected 100 µm sequential sections along the OB DV axis for targeted transcriptomics to determine which ORs were expressed in each section. Canonically, each OR is expressed in two glomeruli per bulb, both of which are expected to be located in similar positions along the DV axis. If

125 enriched OR sequences are from OSN axon terminals, we expect that each OR would be
126 abundant in spatially clustered sections which reflect the OE DV position from which the
127 axons originate.

128 After weighting and normalization across individual mice, the localization pattern of
129 each OR and TAAR was limited to a single spatial cluster in a series of neighboring sections
130 for a majority of the capture-enriched transcripts (Fig. 2, A, B, and C). Uniform Manifold
131 Approximation and Projection (UMAP) (*38*) visualization of data from the three DV replicate
132 mice (22 sections per replicate) placed sequential sections from replicate animals in an
133 ordered, non-clustered path, indicating that spatially related sections have similar
134 transcriptional profiles (Fig. 2D). Replicate heatmaps were similar to each other (mean RV_{adj} =
135 0.1803), which supports the stereotyped targeting of glomeruli to local domains (*39*, *40*). To
136 assess concordance of OB and OE positions along the DV axis, we constructed an
137 expression-weighted mean DV position for each OR from the average of all three DV replicate
138 mice, which we found correlated with the published OE DV positions of each OR (Spearman's
139 rho of mean position and OE index = 0.775, $P < 2.2 \times 10^{-16}$, Spearman's rho = -0.690, $P < 2.2$
140 $\times 10^{-16}$) (Fig. 2E and fig. S2A) (*36*, *37*). Along the DV axis, we found dorsal OE ORs, Class I
141 ORs, and TAARs primarily located in the dorsal OB sections, while Class II ORs were
142 distributed evenly along the DV axis, in agreement with previous mapping studies (dorsal vs
143 ventral $P = 4.292 \times 10^{-95}$, Class I vs Class II $P = 5.912 \times 10^{-20}$, TAAR vs OR $P = 0.0001$,
144 Mann-Whitney U-test) (Fig. 2F) (*29*).
145
146 ***Anteroposterior spatial sections reflect stereotyped targeting of mirror-symmetric***
147 ***glomeruli***

148 Using the same approach as for the DV axis, we examined 100-μm sections along the
149 AP axis of the OB to further assess the precision and reproducibility of our method and the

stereotypical patterning of OR glomeruli. Prior studies have shown that each OR typically has two glomeruli located in distinct, yet spatially linked AP and mediolateral (ML) positions, as each OB is organized into half bulbs along a non-orthogonal symmetry line (*8*, *41*, *42*). This symmetry typically leads to more posterior positioning of the medial glomerulus for an OR. However, in cases where the target location of an OR is close to the symmetry line, both glomeruli may appear in the same AP plane or only a single glomerulus may form (*43*). Based on these studies, we hypothesized that a majority of ORs would exhibit a bimodal expression pattern along the AP axis.

Spatial expression patterns of the normalized transcript abundances for 967 ORs and 14 TAARs were consistent across replicates, with stereotyped AP glomerular positions across OBs (*8*, *44*). When sorted by position of mean expression, ORs primarily displayed two peaks of expression, consistent with published studies for labeled ORs displaying the medial glomerulus in a more posterior location relative to the lateral glomerulus (Fig. 3, A and B, and fig. S3A) (*8*). Compared to the distribution of normalized OR expression across the DV axis, ORs along the AP axis were distributed bimodally (Fig. 3C). Similar to the DV axis, UMAP projections of gene expression values from the six AP replicate mice (23 sections per replicate) revealed correlated expression patterns and AP positions across each OB (Fig. 3D). Across the AP axis, we found Class I ORs biased to the anterior set of sections, while TAARs tended to be localized to the central portion of the axis (Class I vs Class II $P = 2.017 \times 10^{-26}$, TAAR vs OR $P = 0.7882$, Mann-Whitney U-test) (Fig. 3E), consistent with previous studies examining glomeruli labeled in gene-targeted mice (*29*, *45*). We also examined our data for concordance against the set of 32 ORs cloned from the anterior, middle, and posterior sections of an OB from Nakashima et al. (*46*). The ORs cloned from the anterior and middle OB (n = 13) had significantly more anterior mean positions than ORs cloned from the posterior OB (n = 18) (anterior + middle OB cloned ORs vs posterior OB cloned ORs $P =$

0.001, Mann-Whitney U-test) (Fig. 3F and fig. S4A). We further divided these cloned ORs across dorsal OE (n = 11) and ventral OE (n = 20) zones and found that both sets displayed concordance with our AP data, with ORs cloned from the anterior and middle OB positions having a lower AP mean position than ORs cloned from the posterior OB (dorsal OE: anterior and middle OB cloned ORs vs posterior OB cloned ORs $P = 0.1636$, ventral OE: anterior and middle OB cloned ORs vs posterior OB cloned ORs $P = 0.0117$, Mann-Whitney U-test) (fig. S4, B and C).

Relationship of OR sequence and OB position

Gene-targeting approaches have identified a handful of examples in which OR sequence similarity correlates with glomerular position proximity (*24*, *47*). Our dataset with a majority of ORs assigned to specific AP positions allowed us to systematically interrogate whether ORs with similar sequences exhibit similar glomerular positions by computing pairwise alignments for all ORs. To assess this relationship in all dimensions, we additionally generated a ML dataset (3 replicates, 22 sections per replicate) (fig. S5, A to E). Due to the combined presence of Class I ORs, Class II ORs, and TAARs on the dorsal surface of the OB, we separated our analysis into three groups: 1) Class I dorsal OB ORs, 2) Class II dorsal OB ORs, and 3) Class II ventral OB ORs. To assess OR similarity, we defined an OR gene alignment score threshold of 567, which corresponds approximately to the 40% identity threshold used to classify OR genes as belonging to a family (fig. S6A) (*48*). When comparing OR pairs above (≥567) and below (<567) the family-level threshold, we found both Class II dorsal and ventral ORs below the family level threshold displayed significant lower mean interglomerular distances across the AP, DV, and ML axes, suggesting topological relationship between the glomerular positions and family-level OR similarities for Class II ORs (Fig. 4A). In contrast, Class I ORs did not display a consistent relationship between sequence similarity

and mean expression position along the DV and ML axes (median AP distance: 1.42 for ≥567 and 2.18 for <567 $P < 2.2e\text{-}16$, median DV distance: 2.59 for ≥567 and 2.44 for <567 $P = 0.004$, median ML distance: 2.95 for ≥567 and 2.67 for <567 $P = 1.53e^{-5}$, Mann-Whitney U-test) (fig. S6B).

We further examined this relationship by comparing ORs above the 40% (family level ORs), 60% (subfamily level ORs) and 80% (highly similar, used to define OR orthologs) protein identity thresholds (*48*, *49*) using the pairwise alignment score thresholds 993 and 1337 respectively. Comparisons between family (567-993), subfamily (993-1337), and highly similar ORs (>1337) revealed similar results among the Class II ORs (Fig. 4B). Along the AP axis, both dorsal and ventral Class II ORs displayed progressively more similar glomerular positions in groups with higher sequence similarity with statistical significance except for one comparison (Fig. 4B and Table S5). Results for both dorsal and ventral Class II ORs along the DV and ML axes and for Class I ORs along all axes indicated that among the groups of related ORs, glomerular positions typically become more similar or do not change with increasing sequence similarity. Altogether our data generally agrees with a model in which overall similarities of ORs influence the relative glomerular locations.

We next sought to determine if any specific OR amino acid residues correlated with AP position. Due to the different relationships between sequence similarity and OB position for dorsal and ventral ORs, we examined Class II ORs using different cutoffs for the sets of the most anterior and most posterior ORs included in the analysis (20%, 27.5%, 35%) to identify amino acid residues correlating with AP position (Fig. 4C and fig. S7A, B, C). We identified 22 residues whose physicochemical properties differed from all ventral Class II ORs (Fig. 4D and fig. S8C and S9) (*50*). Notably, four consecutive residues that correlated with AP position were in the third intracellular loop, which has been shown to interact directly with the G protein during Class A GPCR activation (Fig. 4, D to F, and fig S8, A and B) (*51*). Additionally,

the phenylalanine within the KAFSTCxSH motif is sandwiched between four residues involved in G-protein binding, (*52*–*54*). These findings indicate residues that are at or near the sites of G-protein interactions are critical in determining glomerular position, which is consistent with the hypothesis that ligand-independent basal activity of ORs influences glomerular targeting (*43*, *46*, *55*–*57*).

A three-dimensional model of OR glomerular positions reflects established features

To systematically estimate OR glomerular positions across the entire OB, we merged our AP, DV, and ML datasets into a unified 3D model. UMAP plots of the mean position of ORs in each dimensional replicate indicated that ORs fall along a 3D axis oriented from anterior-dorsal-medial to posterior-ventral-lateral (fig. S10, A and B). To account for the location of OR glomeruli on the outer surface of the OB, we extracted coordinates from a diffusion tensor imaging (DTI) model of the mouse OB to represent the approximate glomerular layer that would have been sampled by each section along each dimension of our targeted transcriptomics data (*58*). We applied a Bayesian model that computes probability distributions for each OR in each voxel based on the isometric-log ratio transform of the normalized read counts from the corresponding set of intersecting AP, DV, and ML single-dimension samples (*59*, *60*). These normalized counts were weighted by the proportion of TPM of total olfactory marker protein (OMP; expressed in all mature OSNs) originating from that position, normalized by the proportion of voxels located in that section. Finally, we developed an algorithm for the systematic reduction of positional probabilities across the whole OB surface into predicted OR glomerular positions which were then filtered to remove predictions with posterior median values below 0.0005 to account for ORs with low expression. Posterior median summaries for the resulting set of 709 ORs and TAARs in all voxels are freely viewable as interactive 3D maps at kanazian.shinyapps.io/obmap/.

We assessed our algorithm by comparing predictions for Class I and II ORs, dorsal and ventral OE ORs, and the set of ORs examined via transgenic mouse lines by Zapiec et al. (*8*). Predicted glomerular positions for Class I ORs, Class II ORs, and dorsal and ventral ORs were consistent with expectations based on OE zone, OR class, and our single-dimension data (dorsal vs ventral $P = 8.26 \times 10^{-99}$, Class I vs Class II $P = 1.962 \times 10^{-12}$, functional imaging surface enriched vs not-enriched $P = 1.38 \times 10^{-18}$ (see below), Mann-Whitney U-test) (Fig. 5, A and E and fig. S11, C, and D). Additionally, the distribution of predictions for the sets of Class I ORs and TAARs matched previously published findings for target domains (Fig. 5B and fig. 11). Our current model predicts glomerular positions for 700 ORs and 9 TAARs, with predicted positions outperforming randomly selected ORs from the same DV zone and medial/lateral side for the subset of ORs with known positions with a median error of 141 μm (Fig. 5, C and D) (*8*). The relative positions of the Olfr1377 and Olfr881 glomeruli in the gene-targeted mouse lines (see below) were also consistent with those predicted from the spatial transcriptomic data (Fig. 5C and figs. S13 and S14 fig. S12D), providing further support for our three-dimensional glomerular predictions based on the spatial transcriptomic data. In summary, we found our three-dimensional reconstruction of OR glomerular positions to be both in agreement with established OR spatial features and to show greater concordance with these established features than the sets of single-dimension target capture sequencing data alone. Collectively, our results thus provide the first large-scale, unified, and systematic database of OR glomerular positions for the mouse OB.

Identification of ORs within the dorsal functional imaging window

We sought to validate and extend our findings by examining specific ORs that map to glomeruli on the dorsal-central OB surface, which has been extensively characterized by functional imaging in vivo (*9*, *11*, *12*, *44*, *61*). To define the set of ORs accessible under

standard functional imaging approaches, we collected tissue samples from OBs from C57BL6 mice (2 male, 2 female). Each OB was dissected into two parts, one containing the approximate dorsal-central imaging area and the other containing the remainder of the OB (fig. S12A). These 16 samples were processed for target capture sequencing and differential expression analysis to identify ORs enriched in the functional imaging area.

A total of 121 ORs, including 27 Class I ORs and 94 Class II ORs, were consistently enriched in the imaging surface (FDR ≤ 0.05 and LogFC > 0) (Fig. 5B, Fig. S12, B, E and F), with 96% of these ORs known to localize in dorsal OE zones (*36*). We also found nine of the 15 TAARs enriched in the imaging surface, with no TAARs enriched in the remaining OB tissue (fig. S12G), consistent with previous functional imaging of some TAAR glomeruli (*45*). To anatomically and functionally validate our expression analysis, we chose two ORs as targets for the generation of receptor-tagged gene-targeting mouse lines, based on their enrichment in the functional imaging area (Olfr881: FDR = 0.007, LogFC = 2.55 and Olfr1377: FDR = 0.021, LogFC = 2.14) (fig. S12B) and their robust response to the odorant 4-methylacetophenone in pS6-IP RNA-Seq experiments (Olfr1377: FDR = $3.43e^{-26}$, LogFC = 3.18, Olfr881: FDR = $7.37e^{-23}$, LogFC = 3.18). (fig. S12C) (*62*). Using *Easi*-CRISPR (*63*), we inserted *IRES-mKate2* cassettes following the CDS of each OR to create Olfr1377-IRES-mKate2 and Olfr881-IRES-mKate2 mice, in which OSNs expressing either Olfr1377 or Olfr881 also express the cytosolic fluorescent marker mKate2, labeling cell bodies in the OE and glomeruli in the OB (fig. S12D). Whole-mount confocal imaging of the OB in gene-targeted mice revealed mKate2-labeled glomeruli within the dorsal-central OB surface (Fig. 6A and fig. S13, A and B).

Examination of additional whole-mount epifluorescence images allowed us to further assess position and variance of both Olfr1377 and Olfr881 (fig. S14, Fig. 5C). Consistent with the singular expression of most ORs as two mirror-symmetric glomeruli, both gene-targeted

mouse lines labeled two glomeruli per OB. The lateral Olfr1377 glomerulus (n = 10) was positioned centrally along on the AP axis and central-laterally within the ML axis imaging area, while the medial glomerulus (n = 6) was more posterior, ventral, and medial. The lateral Olfr881 glomerulus (n = 9) was positioned centrally along the ML axis and relatively posterior within the imaging area, while the medial glomerulus (n = 8) displayed a more variable position across the medioposterior quarter of the dorsal surface. The lateral Olfr1377 glomerulus displayed nearly twice (196.8%) the positional variance than the lateral Olfr881 glomerulus while the medial Olfr1377 glomerulus was distributed in an area nearly half the size (52.8%) of its Olfr881 counterpart.

Functional imaging of dorsal ORs

Expression of long-wavelength mKate2 as an OR-specific marker allowed for functional characterization of Olfr1377 and Olfr881 glomeruli by crossing the generated mouse lines to OSN-specific driver lines expressing a GCaMP Ca^{2+} reporter. For maximal imaging sensitivity, we crossed each mKate2 line to the OMP-IRES-tTA driver line (*64*) and the tetO-GCaMP6s reporter line (*65*). In the resulting triple crosses, we readily located the lateral mKate2-tagged glomeruli on the dorsal functional imaging surface (Fig. 6A) and imaged odorant-evoked GCaMP6s signals from these and neighboring glomeruli using dual-wavelength two-photon imaging in anesthetized mice. Consistent with our pS6-IP in vivo data (fig. S12C), both Olfr1377 and Olfr881 exhibited robust responses to low concentrations of 4-methylacetophenone, with Olfr1377 exhibiting a stronger response than Olfr881 (Fig. 6, B and C). In addition to 4-methylacetophenone, we also tested a large odorant panel including multiple cyclic ketones structurally related to 4-methylacetophenone, as well as more diverse odorants, all at relatively low concentrations. From this panel, we identified multiple new, high-affinity ligands for each OR, including many cyclic ketones, and ultimately uncovered

overlapping but distinct response spectra for Olfr1377 and Olfr881 (Fig. 6C, fig. S15C). For example, Olfr1377 showed strong responses to p-anisaldehyde, acetophenone, and the aliphatic ketone 4-methyl-3-penten-2-one, while Olfr881 proved unresponsive to these odorants.

Interestingly, Olfr1377 (but not Olfr881) exhibited an exceptionally strong response to 4-methoxyacetophenone, with a brief (2 s) presentation of ~0.4 nM 4-methoxyacetophenone eliciting long-term activation and desensitization (fig. S15, A and B). Additional concentration screening suggested an in vivo response threshold of ~10^{-13} M 4-methoxyacetophenone for the Olfr1377 glomerulus (Fig. 6D and fig. S15D). To complement our in vivo imaging and pS6-IP RNA-Seq analyses and further evaluate the sensitivity of Olfr1377 to 4-methylacetophenone and 4-methoxyacetphenone, we additionally expressed Olfr1377 in Hana3a cells and examined luciferase responses to different concentrations of 4-methoxyacetophenone, 4-methylacetophenone, 2'-hydroxyacetophenone, and acetophenone (*66*, *67*). Reinforcing our in vivo results, Olfr1377 responded to all four odorants (Fig. 6E). Moreover, Olfr1377 responded to 4-methoxyacetophenone at just 1 nM and saturated at 100 nM in vitro, a response orders-of-magnitude more sensitive than the response to any other odorant tested. Collectively, these findings thus identify 4-methoxyacetophenone-Olfr1377 as a ligand-receptor interaction with exceptionally high affinity.

DISCUSSION

Olfactory receptor neurons in *Drosophila* predominantly express a single OR out of a repertoire of 62 OR genes and project their axons to one of ~50 distinct glomeruli on each antennal lobe (*68*, *69*). These glomeruli have been individually linked to specific ORs, allowing for a complete picture of how sensory information is organized within the first olfactory relay (*69*–*71*). This key map has served as a foundation for critical studies regarding

sensory processing, olfactory receptor neuron-targeting factors, the propagation of information to higher-order neurons, and the cellular composition of the antennal lobe (*72*–*75*). In contrast, the mammalian system involves over an order of magnitude more receptors and lacks such a comprehensive and specific mapping.

With over 1000 ORs projecting to approximately 1800 glomeruli arrayed over the three-dimensional surface of the mouse OB, the experimental challenge of mapping ORs to glomeruli is profound (*76*). To date, such mapping in the mouse has relied primarily on the creation of gene-targeted animals or in situ hybridization of radiolabeled probes. Further, the lack of finescale landmarks within the OB and differences between methods used to identify glomerular positions has led to relatively limited comparable positional information, with single studies examining just six ORs by in situ hybridization and five by fluorescent markers (*8*, *26*). Given the low-throughput of these previous assays and the large size of the mouse OR repertoire, the ability of the field to comprehensively assess the genetic and logical organization of the olfactory map has been limited.

Here, we demonstrate a unique application of target capture sequencing, enriching low-abundance target transcripts found in the axon terminals of sensory neurons and comparing post-enrichment abundances between samples. We applied this method to 100 µm sections along the three cardinal axes to circumvent a longstanding problem in olfaction: resolving the receptor organization of the olfactory map. Our high-throughput approach generated the first repertoire-scale dataset for OR glomerular positions and enabled the creation of a three-dimensional positional estimate for the glomeruli of a majority of the OR repertoire with an approximate precision within ranges previously observed for positional variability between animals. The scale of our study enabled us to verify the longstanding observation that OE zones map directly to OB glomeruli along the dorsoventral axis. Additionally, our dataset allowed us to begin interrogating how OR sequence is related to OB

target position, an important aspect for the formation of the olfactory map. We found that, in general, OR sequence similarity correlates with OB target position for both classes of ORs and for both the dorsal and ventral hemispheres of the OB. Targeting along the AP axis has further been hypothesized to be associated with ligand-independent basal activity of the OR protein located at the axon terminal membrane. We defined a set of amino acid residues correlated with the most-anterior and most-posterior ventral Class II ORs. Intriguingly, many of these residues were proximal to domains involved in G-protein coupling, which raises the possibility for involvement in modulation of basal activity levels, which would in turn influence targeting along the AP axis. Mutational studies testing a diverse set of ORs in both in vitro and in vivo paradigms will likely be needed to determine the exact effect of each residue as basal activity is dependent on the OR, secondary structure interactions, and the membrane the receptor is embedded within.

While our data lacks single glomerulus-level spatial resolution, our three-dimensional model provides a probabilistic model of OR glomerular positions that leverages biological replicates and glomerular position stereotypy. We provide a visualization of the most likely voxel for a given glomerulus and high probability voxels indicating the potential variance in position. We provide predictions for all 980 ORs and TAARs analyzed in our single-dimension heatmaps in an online application where we provide an interactive model with values and filters for probabilities of our predictions.

In developing this three-dimensional model, we also identified the set of ORs and TAARs present within the dorsal surface that is typically viewed in functional imaging studies, which, almost exclusively, lack information regarding the OR identity of the observed glomerular responses. Identification of this set, representing ~10% of the OR repertoire, will directly facilitate the in vivo deorphanization of ORs by guiding combined gene-targeting and functional imaging approaches – a strategy crucial for validating and fine-tuning

complementary in vitro deorphanization screens (*13*, *77*). Using this approach, we identified numerous ligands for two previously uncharacterized ORs - Olfr881 and Olfr1377 - including odorants activating both receptors (e.g., 4-methylacetophenone; methyl isoeugenol) as well as odorants selectively activating only Olfr881 (e.g., menthone) or Olfr1377 (e.g., p-anisaldehyde). In addition, we uncovered an exceptionally sensitive and long-lasting response of Olfr1377 to 4-methoxyacetophenone, with affinity paralleling the ultrasensitive detection of amines by TAARs (*77*). Of great interest, this latter result tentatively suggests that high-affinity odorant-receptor interactions are not exclusively limited to TAARs and physiologically important amines, but may exist for a broader collection of ORs and diverse odorants.

The projection of OSN axons from the OE to OB glomeruli requires exquisite accuracy and precision. The degree of inter-individual variation requires replicate animals to be sampled and limits the precision to which any approach can achieve, and our approach provides a level of precision that is comparable to the resolution limits set by stereotyped targeting. The mapping of OR glomerular positions to specific subdomains of the OB broadly serves to generate unique insights into how this early sensory relay center is organized and reflects our chemical environment. Joining ligand-receptor deorphanization data with our newly generated OR-OB positional data enables large-scale investigations into how representations of odor space relate to topographical features in the OB and facilitates the development of unified, systematic models for how chemical inputs are processed, interpreted, and transformed into odor-driven behaviors.

REFERENCES:

1. L. B. Buck, Information coding in the vertebrate olfactory system. *Annu. Rev. Neurosci.* **19**, 517–544 (1996).
2. H. Takeuchi, H. Sakano, Neural map formation in the mouse olfactory system. *Cell. Mol. Life Sci.* **71**, 3049–3057 (2014).
3. S. M. Potter, C. Zheng, D. S. Koos, P. Feinstein, S. E. Fraser, P. Mombaerts, Structure and emergence of specific olfactory glomeruli in the mouse. *J. Neurosci.* **21**, 9713–9723 (2001).
4. A. J. Pinching, T. P. Powell, The neuropil of the glomeruli of the olfactory bulb. *J. Cell Sci.* **9**, 347–377 (1971).
5. K. J. Ressler, S. L. Sullivan, L. B. Buck, Information coding in the olfactory system: Evidence for a stereotyped and highly organized epitope map in the olfactory bulb. *Cell*. **79**, 1245–1255 (1994).
6. R. Vassar, S. K. Chao, R. Sitcheran, J. M. Nuñez, L. B. Vosshall, R. Axel, Topographic organization of sensory projections to the olfactory bulb. *Cell*. **79**, 981–991 (1994).
7. P. Mombaerts, F. Wang, C. Dulac, S. K. Chao, A. Nemes, M. Mendelsohn, J. Edmondson, R. Axel, Visualizing an olfactory sensory map. *Cell*. **87**, 675–686 (1996).
8. B. Zapiec, P. Mombaerts, Multiplex assessment of the positions of odorant receptor-specific glomeruli in the mouse olfactory bulb by serial two-photon tomography. *Proc. Natl. Acad. Sci.* **112**, E5873-5882 (2015).
9. B. D. Rubin, L. C. Katz, Optical imaging of odorant representations in the mammalian olfactory bulb. *Neuron*. **23**, 499–511 (1999).
10. R. W. Friedrich, S. I. Korsching, Combinatorial and Chemotopic Odorant Coding in the Zebrafish Olfactory Bulb Visualized by Optical Imaging. *Neuron*. **18**, 737–752 (1997).
11. M. Wachowiak, L. B. Cohen, Representation of odorants by receptor neuron input to the

446 mouse olfactory bulb. *Neuron*. **32**, 723–735 (2001).

447 12. T. Bozza, J. P. McGann, P. Mombaerts, M. Wachowiak, In vivo imaging of neuronal
448 activity by targeted expression of a genetically encoded probe in the mouse. *Neuron*.
449 **42**, 9–21 (2004).

450 13. Y. Oka, S. Katada, M. Omura, M. Suwa, Y. Yoshihara, K. Touhara, Odorant Receptor
451 Map in the Mouse Olfactory Bulb: In Vivo Sensitivity and Specificity of Receptor-Defined
452 Glomeruli. *Neuron*. **52**, 857–869 (2006).

453 14. C. Zheng, P. Feinstein, T. Bozza, I. Rodriguez, P. Mombaerts, Peripheral Olfactory
454 Projections Are Differentially Affected in Mice Deficient in a Cyclic Nucleotide-Gated
455 Channel Subunit. *Neuron*. **26**, 81–91 (2000).

456 15. M. Smear, A. Resulaj, J. Zhang, T. Bozza, D. Rinberg, Multiple perceptible signals from
457 a single olfactory glomerulus. *Nat. Neurosci.* **16**, 1687–1691 (2013).

458 16. J. Strotmann, S. Conzelmann, A. Beck, P. Feinstein, H. Breer, P. Mombaerts, Local
459 permutations in the glomerular array of the mouse olfactory bulb. *J. Neurosci.* **20**,
460 6927–6938 (2000).

461 17. C. D. Hulst, R. B. Mina, Z. Gershon, M. E. Rogers, Y. Sirotin, P. Feinstein, C. D. Hulst,
462 R. B. Mina, Z. Gershon, S. Jamet, A. Cerullo, D. Tomoiaga, MouSensor : A Versatile
463 Genetic Platform to Create Super Sniffer Mice for Studying Human Odor Coding Article
464 MouSensor : A Versatile Genetic Platform to Create Super Sniffer Mice for Studying
465 Human Odor Coding. *Cell Rep.* **16**, 1–11 (2016).

466 18. T. Bozza, P. Feinstein, C. Zheng, P. Mombaerts, Odorant receptor expression defines
467 functional units in the mouse olfactory system. *J. Neurosci.* **22**, 3033–3043 (2002).

468 19. X. Grosmaitre, S. H. Fuss, A. C. Lee, K. a Adipietro, H. Matsunami, P. Mombaerts, M.
469 Ma, SR1, a mouse odorant receptor with an unusually broad response profile. *J.*
470 *Neurosci.* **29**, 14545–52 (2009).

20. M. Shirasu, K. Yoshikawa, Y. Takai, A. Nakashima, H. Takeuchi, H. Sakano, K. Touhara, Olfactory receptor and neural pathway responsible for highly selective sensing of musk odors. *Neuron*. **81**, 165–178 (2014).

21. H. Saito, H. Nishizumi, S. Suzuki, H. Matsumoto, N. Ieki, T. Abe, H. Kiyonari, M. Morita, H. Yokota, N. Hirayama, T. Yamazaki, T. Kikusui, K. Mori, H. Sakano, Immobility responses are induced by photoactivation of single glomerular species responsive to fox odour TMT. *Nat. Commun.* **8**, 1–10 (2017).

22. A. Mizrahi, H. Matsunami, L. C. Katz, An imaging-based approach to identify ligands for olfactory receptors. *Neuropharmacology*. **47**, 661–668 (2004).

23. K. Miyamichi, S. Serizawa, H. Kimura, H. Sakano, Continuous and Overlapping Expression Domains of Odorant Receptor Genes in the Olfactory Epithelium Determine the Dorsal/Ventral Positioning of Glomeruli in the Olfactory Bulb. *J. Neurosci.* **25**, 3586–3592 (2005).

24. P. Feinstein, T. Bozza, I. Rodriguez, A. Vassalli, P. Mombaerts, Axon guidance of mouse olfactory sensory neurons by odorant receptors and the B2AR. *Cell*. **117**, 833–846 (2004).

25. J. Li, T. Ishii, P. Feinstein, P. Mombaerts, Odorant receptor gene choice is reset by nuclear transfer from mouse olfactory sensory neurons. *Nature*. **428**, 393–399 (2004).

26. A. Tsuboi, T. Miyazaki, T. Imai, H. Sakano, Olfactory sensory neurons expressing class I odorant receptors converge their axons on an antero-dorsal domain of the olfactory bulb in the mouse. *Eur. J. Neurosci.* **23**, 1436–1444 (2006).

27. A. Tsuboi, S. Yoshihara, N. Yamazaki, H. Kasai, H. Asai-Tsuboi, M. Komatsu, S. Serizawa, T. Ishii, Y. Matsuda, F. Nagawa, H. Sakano, Olfactory neurons expressing closely linked and homologous odorant receptor genes tend to project their axons to neighboring glomeruli on the olfactory bulb. *J. Neurosci.* **19**, 8409–8418 (1999).

28. S. Serizawa, T. Ishii, H. Nakatani, A. Tsuboi, F. Nagawa, M. Asano, K. Sudo, J. Sakagami, H. Sakano, T. Ijiri, Y. Matsuda, M. Suzuki, T. Yamamori, Y. Iwakura, H. Sakano, Mutually exclusive expression of odorant receptor transgenes. *Nat. Neurosci.* **3**, 687–693 (2000).

29. T. Bozza, A. Vassalli, S. Fuss, J. J. Zhang, B. Weiland, R. Pacifico, P. Feinstein, P. Mombaerts, Mapping of Class I and Class II Odorant Receptors to Glomerular Domains by Two Distinct Types of Olfactory Sensory Neurons in the Mouse. *Neuron*. **61**, 220–233 (2009).

30. A. Mortazavi, B. A. Williams, K. McCue, L. Schaeffer, B. Wold, Mapping and quantifying mammalian transcriptomes by RNA-Seq. *Nat. Methods*. **5**, 621–628 (2008).

31. D.-J. Zou, P. Feinstein, A. Rivers, G. Mathews, A. Kim, C. Greer, P. Mombaerts, S. Firestein, Postnatal Refinement of Peripheral Olfactory Projections. *Science.* **304**, 1976–1979 (2004).

32. T. R. Mercer, M. B. Clark, J. Crawford, M. E. Brunck, D. J. Gerhardt, R. J. Taft, L. K. Nielsen, M. E. Dinger, J. S. Mattick, Targeted sequencing for gene discovery and quantification using RNA CaptureSeq. *Nat. Protoc.* **9**, 989–1009 (2014).

33. K. J. Ressler, S. L. Sullivan, L. B. Buck, A zonal organization of odorant receptor gene expression in the olfactory epithelium. *Cell*. **73**, 597–609 (1993).

34. R. Vassar, J. Ngai, R. Axel, Spatial segregation of odorant receptor expression in the mammalian olfactory epithelium. *Cell*. **74**, 309–318 (1993).

35. L. Astic, D. Saucier, Anatomical mapping of the neuroepithelial projection to the olfactory bulb in the rat. *Brain Res. Bull.* **16**, 445–454 (1986).

36. L. Tan, X. S. Xie, A near-complete spatial map of olfactory receptors in the mouse main olfactory epithelium. *Chem. Senses*. **43**, 427–432 (2018).

37. B. Zapiec, P. Mombaerts, The Zonal Organization of Odorant Receptor Gene Choice in

the Main Olfactory Epithelium of the Mouse. *Cell Rep.* **30**, 4220–4234 (2020).

38. E. Becht, L. McInnes, J. Healy, C. A. Dutertre, I. W. H. Kwok, L. G. Ng, F. Ginhoux, E. W. Newell, Dimensionality reduction for visualizing single-cell data using UMAP. *Nat. Biotechnol.* **37**, 38–47 (2019).

39. M. L. Schaefer, T. E. Finger, D. Restrepo, Variability of position of the P2 glomerulus within a map of the mouse olfactory bulb. *J. Comp. Neurol.* **436**, 351–362 (2001).

40. C. D. Mayer, J. Lorent, G. W. Horgan, Exploratory analysis of multiple omics datasets using the adjusted RV coefficient. *Stat. Appl. Genet. Mol. Biol.* **10** (2011).

41. K. Mori, H. Sakano, How is the olfactory map formed and interpreted in the mammalian brain? *Annu. Rev. Neurosci.* **34**, 467–499 (2011).

42. V. N. Murthy, Olfactory maps in the brain. *Annu. Rev. Neurosci.* **34**, 233–258 (2011).

43. B. Zapiec, O. Christian Bressel, M. Khan, A. Walz, P. Mombaerts, Neuropilin-1 and the Positions of Glomeruli in the Mouse Olfactory Bulb. *eNeuro*. **3**, 1–19 (2016).

44. E. Soucy, D. Albeanu, F. Antoniu, V. Murthy, M. Meister, Precision and diversity in an odor map on the olfactory bulb. *Nat. Neurosci.* **12**, 1351–1360 (2009).

45. R. Pacifico, A. Dewan, D. Cawley, C. Guo, T. Bozza, An olfactory subsystem that mediates high-sensitivity detection of volatile amines. *Cell Rep.* **2**, 76–88 (2012).

46. A. Nakashima, H. Takeuchi, T. Imai, H. Saito, H. Kiyonari, T. Abe, M. Chen, L. S. Weinstein, C. R. Yu, D. R. Storm, H. Nishizumi, H. Sakano, Agonist-independent GPCR activity regulates anterior-posterior targeting of olfactory sensory neurons. *Cell*. **154**, 1314–1325 (2013).

47. F. Wang, A. Nemes, M. Mendelsohn, R. Axel, Odorant Receptors Govern the Formation of a Precise Topographic Map. *Cell*. **93**, 47–60 (1998).

48. G. Glusman, A. Bahar, D. Sharon, Y. Pilpel, J. White, D. Lancet, The olfactory receptor gene superfamily: Data mining, classification, and nomenclature. *Mamm. Genome*. **11**,

1016–1023 (2000).

49. T. Olender, T. E. M. Jones, E. Bruford, D. Lancet, A unified nomenclature for vertebrate olfactory receptors. *BMC Evol. Biol.* **20**, 1–12 (2020).

50. R. Grantham, Amino Acid Difference Formula to Help Explain Protein Evolution. *Science.* **185**, 862–864 (1974).

51. S. G. F. Rasmussen, B. T. Devree, Y. Zou, A. C. Kruse, K. Y. Chung, T. S. Kobilka, F. S. Thian, P. S. Chae, E. Pardon, D. Calinski, J. M. Mathiesen, S. T. A. Shah, J. A. Lyons, M. Caffrey, S. H. Gellman, J. Steyaert, G. Skiniotis, W. I. Weis, R. K. Sunahara, B. K. Kobilka, Crystal structure of the β 2 adrenergic receptor-Gs protein complex. *Nature*. **477**, 549–557 (2011).

52. A. Kato, S. Katada, K. Touhara, Amino acids involved in conformational dynamics and G protein coupling of an odorant receptor: Targeting gain-of-function mutation. *J. Neurochem.* **107**, 1261–1270 (2008).

53. A. Kato, K. Touhara, Mammalian olfactory receptors: Pharmacology, G protein coupling and desensitization. *Cell. Mol. Life Sci.* **66**, 3743–3753 (2009).

54. C. A. De March, S. K. Kim, S. Antonczak, W. A. Goddard, J. Golebiowski, G protein-coupled odorant receptors: From sequence to structure. *Protein Sci.* **24**, 1543–1548 (2015).

55. T. Imai, M. Suzuki, H. Sakano, Odorant Receptor-Derived cAMP Signals Direct Axonal Targeting. *Science.* **313**, 667–669 (2006).

56. T. Imai, T. Yamazaki, R. Kobayakawa, K. Kobayakawa, T. Abe, M. Suzuku, H. Sakano, Pre-Target Axon Sorting Establishes the Neural Map Topography. *Science.* **17**, 585–590 (2009).

57. A. Assens, J. A. Dal Col, A. Njoku, Q. Dietschi, C. Kan, P. Feinstein, A. Carleton, I. Rodriguez, Alteration of Nrp1 signaling at different stages of olfactory neuron

maturation promotes glomerular shifts along distinct axes in the olfactory bulb. *Development*. **143**, 3817–3825 (2016).

58. G. A. Johnson, A. Badea, J. Brandenburg, G. Cofer, B. Fubara, S. Liu, J. Nissanov, Waxholm Space: An image-based reference for coordinating mouse brain research. *Neuroimage*. **53**, 365–372 (2010).

59. J. J. Egozcue, V. Pawlowsky-Glahn, G. Mateu-Figueras, C. Barceló-Vidal, Isometric Logratio Transformations for Compositional Data Analysis. *Math. Geol.* **35**, 279–300 (2003).

60. J. D. Silverman, A. D. Washburne, S. Mukherjee, L. A. David, A phylogenetic transform enhances analysis of compositional microbiota data. *Elife*. **6**, 1–20 (2017).

61. M. Ma, G. M. Shepherd, Functional mosaic organization of mouse olfactory receptor neurons. *Proc. Natl. Acad. Sci. U. S. A.* **97**, 12869–12874 (2000).

62. Y. Jiang, N. N. Gong, X. S. Hu, M. J. Ni, R. Pasi, H. Matsunami, Molecular profiling of activated olfactory neurons identifies odorant receptors responding to odors in vivo. *Nat. Neurosci.* **18**, 1446–54 (2015).

63. R. M. Quadros, H. Miura, D. W. Harms, H. Akatsuka, T. Sato, T. Aida, R. Redder, G. P. Richardson, Y. Inagaki, D. Sakai, S. M. Buckley, P. Seshacharyulu, S. K. Batra, M. A. Behlke, S. A. Zeiner, A. M. Jacobi, Y. Izu, W. B. Thoreson, L. D. Urness, S. L. Mansour, M. Ohtsuka, C. B. Gurumurthy, Easi-CRISPR: A robust method for one-step generation of mice carrying conditional and insertion alleles using long ssDNA donors and CRISPR ribonucleoproteins. *Genome Biol.* **18**, 1–15 (2017).

64. C. R. Yu, J. Power, G. Barnea, S. O'Donnell, H. E. V. Brown, J. Osborne, R. Axel, J. A. Gogos, Spontaneous neural activity is required for the establishment and maintenance of the olfactory sensory map. *Neuron*. **42**, 553–566 (2004).

65. J. B. Wekselblatt, E. D. Flister, D. M. Piscopo, C. M. Niell, Large-scale imaging of

596 cortical dynamics during sensory perception and behavior. *J. Neurophysiol.* **115**, 2852–
597 2866 (2016).
598 66. H. Saito, M. Kubota, R. W. Roberts, Q. Chi, H. Matsunami, RTP family members induce
599 functional expression of mammalian odorant receptors. *Cell*. **119**, 679–691 (2004).
600 67. H. Zhuang, H. Matsunami, Evaluating cell-surface expression and measuring activation
601 of mammalian odorant receptors in heterologous cells. *Nat. Protoc.* **3**, 1402–1413
602 (2008).
603 68. L. B. Vosshall, R. F. Stocker, Molecular architecture of smell and taste in Drosophila.
604 *Annu. Rev. Neurosci.* **30**, 505–533 (2007).
605 69. V. Grabe, A. Strutz, A. Baschwitz, B. S. Hansson, S. Sachse, Digital in vivo 3D atlas of
606 the antennal lobe of Drosophila melanogaster. *J. Comp. Neurol.* **523**, 530–544 (2015).
607 70. P. P. Laissue, C. Reiter, P. R. Hiesinger, S. Halter, K. F. Fischbach, R. F. Stocker,
608 Three-Dimensional Reconstruction of the Antennal Lobe in. *J. Comp. Neurol.* **552**, 543–
609 552 (1999).
610 71. E. A. Hallem, J. R. Carlson, Coding of Odors by a Receptor Repertoire. *Cell*. **125**, 143–
611 160 (2006).
612 72. Y. H. Chou, M. L. Spletter, E. Yaksi, J. C. S. Leong, R. I. Wilson, L. Luo, Diversity and
613 wiring variability of olfactory local interneurons in the Drosophila antennal lobe. *Nat.*
614 *Neurosci.* **13**, 439–449 (2010).
615 73. S. R. Olsen, V. Bhandawat, R. I. Wilson, Divisive normalization in olfactory population
616 codes. *Neuron*. **66**, 287–299 (2010).
617 74. J. M. Jeanne, M. Fişek, R. I. Wilson, The Organization of Projections from Olfactory
618 Glomeruli onto Higher-Order Neurons. *Neuron*. **98**, 1198-1213.e6 (2018).
619 75. N. K. Tanaka, K. Endo, K. Ito, Organization of antennal lobe-associated neurons in
620 adult Drosophila melanogaster brain. *J. Comp. Neurol.* **520**, 4067–4130 (2012).

621 76. J. P. Royet, C. Souchier, F. Jourdan, H. Ploye, Morphometric study of the glomerular
622 population in the mouse olfactory bulb: numerical density and size distribution along the
623 rostrocaudal axis. *J. Comp. Neurol.* **270**, 559–68 (1988).
624 77. J. Zhang, R. Pacifico, D. Cawley, P. Feinstein, T. Bozza, Ultrasensitive detection of
625 amines by a trace amine-associated receptor. *J. Neurosci.* **33**, 3228–3239 (2013).
626 78. J. Köster, S. Rahmann, Snakemake-a scalable bioinformatics workflow engine.
627 *Bioinformatics*. **28**, 2520–2522 (2012).
628 79. A. Dobin, C. A. Davis, F. Schlesinger, J. Drenkow, C. Zaleski, S. Jha, P. Batut, M.
629 Chaisson, T. R. Gingeras, STAR: Ultrafast universal RNA-seq aligner. *Bioinformatics*.
630 **29**, 15–21 (2013).
631 80. B. Li, C. N. Dewey, RSEM: accurate transcript quantification from RNA-Seq data with or
632 without a reference genome. *BMC Bioinformatics*. **12**, 323 (2011).
633 81. T. Olender, N. Nativ, D. Lancet, "HORDE: Comprehensive Resource for Olfactory
634 Receptor Genomics" in *Olfactory Receptors: Methods and Protocols*, C. J. Crasto, Ed.
635 (Humana Press, Totowa, NJ, 2013), pp. 23–38.
636 82. D. J. McCarthy, Y. Chen, G. K. Smyth, Differential expression analysis of multifactor
637 RNA-Seq experiments with respect to biological variation. *Nucleic Acids Res.* **40**, 4288–
638 4297 (2012).
639 83. C. A. de March, J. Topin, E. Bruguera, G. Novikov, K. Ikegami, H. Matsunami, J.
640 Golebiowski, Odorant Receptor 7D4 Activation Dynamics. *Angew. Chemie - Int. Ed.* **57**,
641 4554–4558 (2018).
642 84. H. Zhuang, H. Matsunami, Synergism of accessory factors in functional expression of
643 mammalian odorant receptors. *J. Biol. Chem.* **282**, 15284–15293 (2007).
644 85. H. Saito, Q. Chi, H. Zhuang, H. Matsunami, J. D. Mainland, Odor coding by a
645 Mammalian receptor repertoire. *Sci. Signal.* **2**, ra9–ra9 (2009).

646

ACKNOWLEDGMENTS:

We thank members of the Matsunami lab for thoughtful discussions and feedback. Luis R. Saraiva (SIDRA Institute), Antonio Scialdone (Helmholtz Zentrum München), and Mayra L. Ruiz Tejada Segura (Helmholtz Zentrum München) provided helpful advice on mapping OR expression and spatial transcriptomics. We thank Sayan Mukherjee (Duke University) for guidance on the combination of single dimension transcriptomic data into a three dimensional model. We thank C. Ron Yu (Stowers Institute, Univ. of Kansas) for providing OMP-IRES-tTA mice. We thank Shelby Priest (Duke University) for assistance with critical reading and feedback.

FUNDING

National Science Foundation grant 1555919 (MW, HM)

National Institute of Neurological Disorders and Stroke grant R01NS109979 (MW)

National Institutes of Health grant 1F31DC017394-03A1 (KWZ)

National Institute of Mental Health grant F32MH115448 (SDB)

National Institutes of Health grant K99DC018333-01 (CAdM)

AUTHOR CONTRIBUTIONS

Conceptualization: KWZ, MW, HM

Methodology: KWZ, SDB, JDS, MW, HM

Investigation: KWZ, SDB, MHN, MW, HM

Visualization: KWZ, SDB, MHN, CAdM, MW, HM

Funding acquisition: KWZ, SDB, MW, HM

Project administration: MW, HM

Supervision: MW, HM

672 Writing – original draft: KWZ, SDB, MW, HM

673 Writing – review & editing: KWZ, SDB, MHN, JDS, CAdM, MW, HM

674

675 **COMPETING INTERESTS**

676 Authors declare that they have no competing interests.

677

678 **DATA AND MATERIALS AVAILABILITY**

679 All data are available in the main text or the supplemental materials.

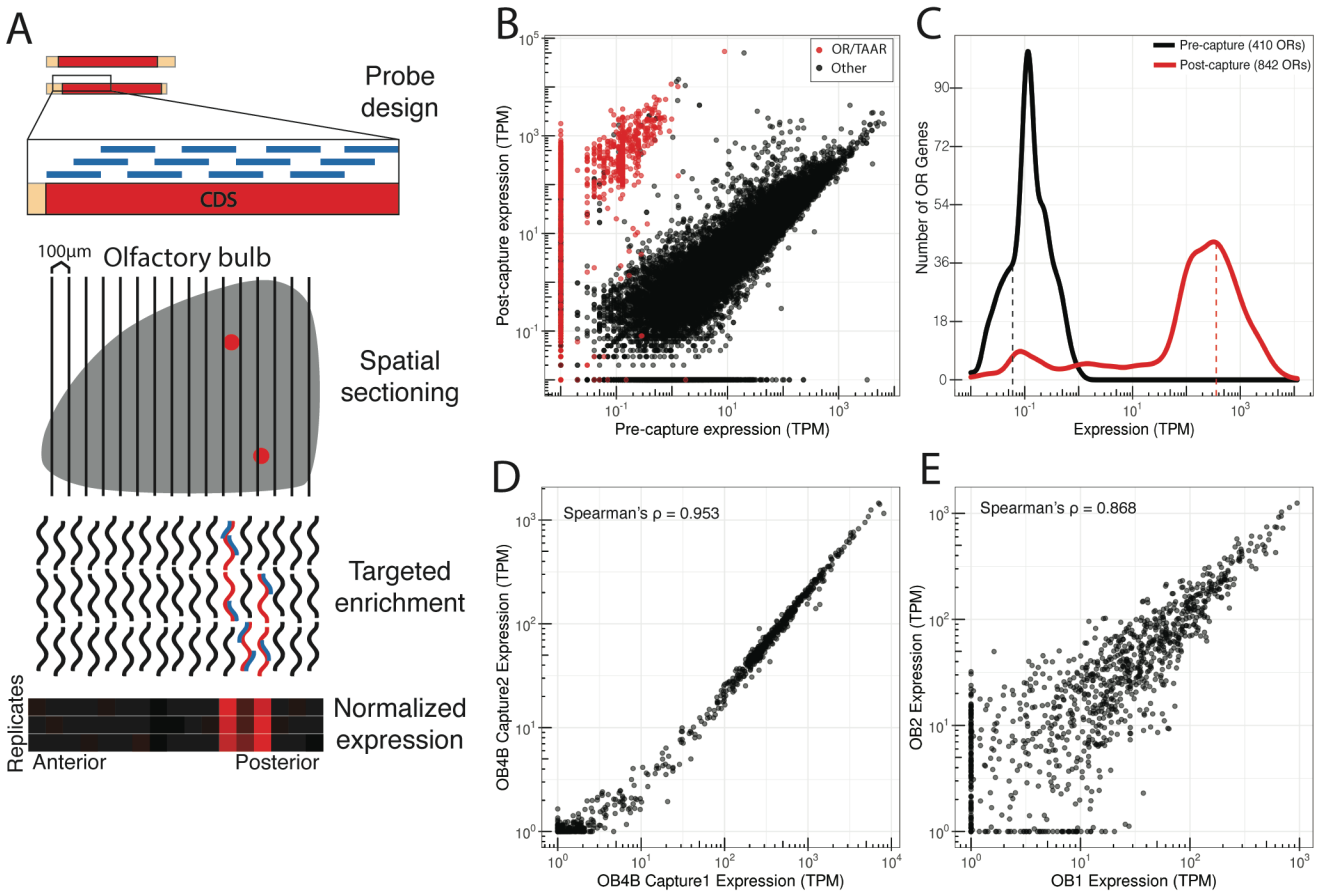

Fig. 1. Target capture sequencing consistently enriches OR transcripts. (**A**) Methodological overview for targeted enrichment of OR and TAAR transcripts from OB sections. Briefly, RNA is extracted from OB tissue and used for cDNA synthesis and library preparation. Capture probes are designed against coding sequences (CDS) of interest, enabling enrichment of target genes following binding and washing steps. RNA-Seq of enriched libraries allows for high-throughput positional analyses when combined with systematic tissue sectioning. (**B**) Pre- and post-capture normalized abundances (transcripts per million; TPM) of intact OR and TAAR genes (red) and other intact genes (black) from a whole OB. (**C**) Frequency distribution of OR gene abundances pre- and post-capture from a whole OB. (**D**) Technical replicates demonstrating OR and TAAR gene abundances from independent capture enrichments of the same whole-OB RNA. (**E**) Biological replicates

demonstrating OR and TAAR gene abundances from capture enrichment of whole-OB RNA samples from different animals.

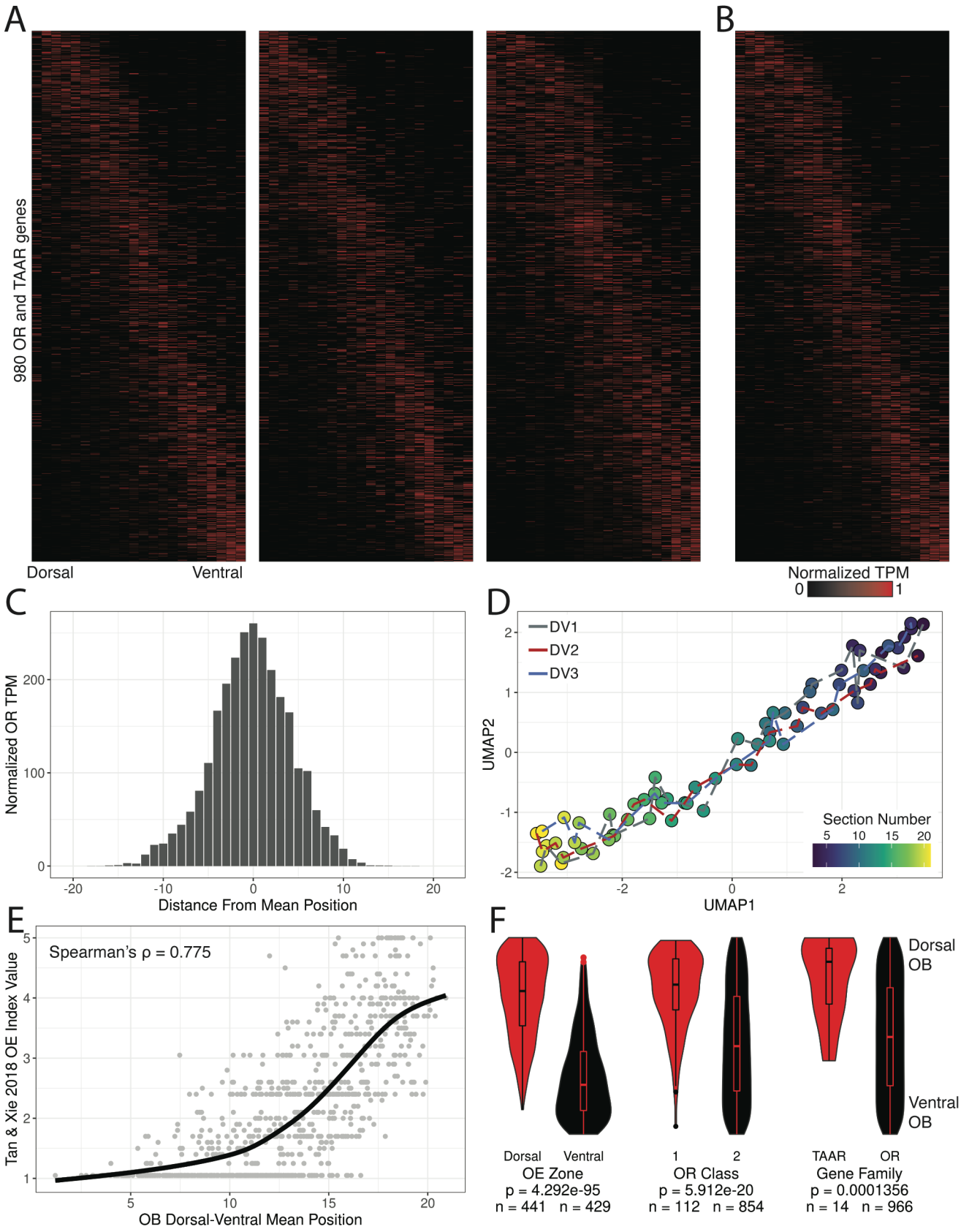

Fig. 2. Glomerular OR expression correlates with OE expression along the DV axis. (**A**)

Heatmaps for 980 ORs and TAARs across 22 DV sections sorted by mean position of expression from three replicate mice. (**B**) Merged representation of DV replicates. Ordering of genes (Y axis) is consistent across all heatmaps. (**C**) Distribution of normalized TPM (maximum observed value = 1, minimum observed value = 0) for all 980 ORs and TAARs from position of mean expression. (**D**) UMAP projection of 22 DV sections from all three replicates. (**E**) Line is loess smoothed regression of OE DV index from Tan and Xie, *Chem. Senses* 2018 across DV mean positions from our targeted spatial data. (**F**) Distribution of ranked DV mean positions for the 980 ORs and TAARs by OE zone, OR class, and gene family. Statistic is Mann-Whitney U-test.

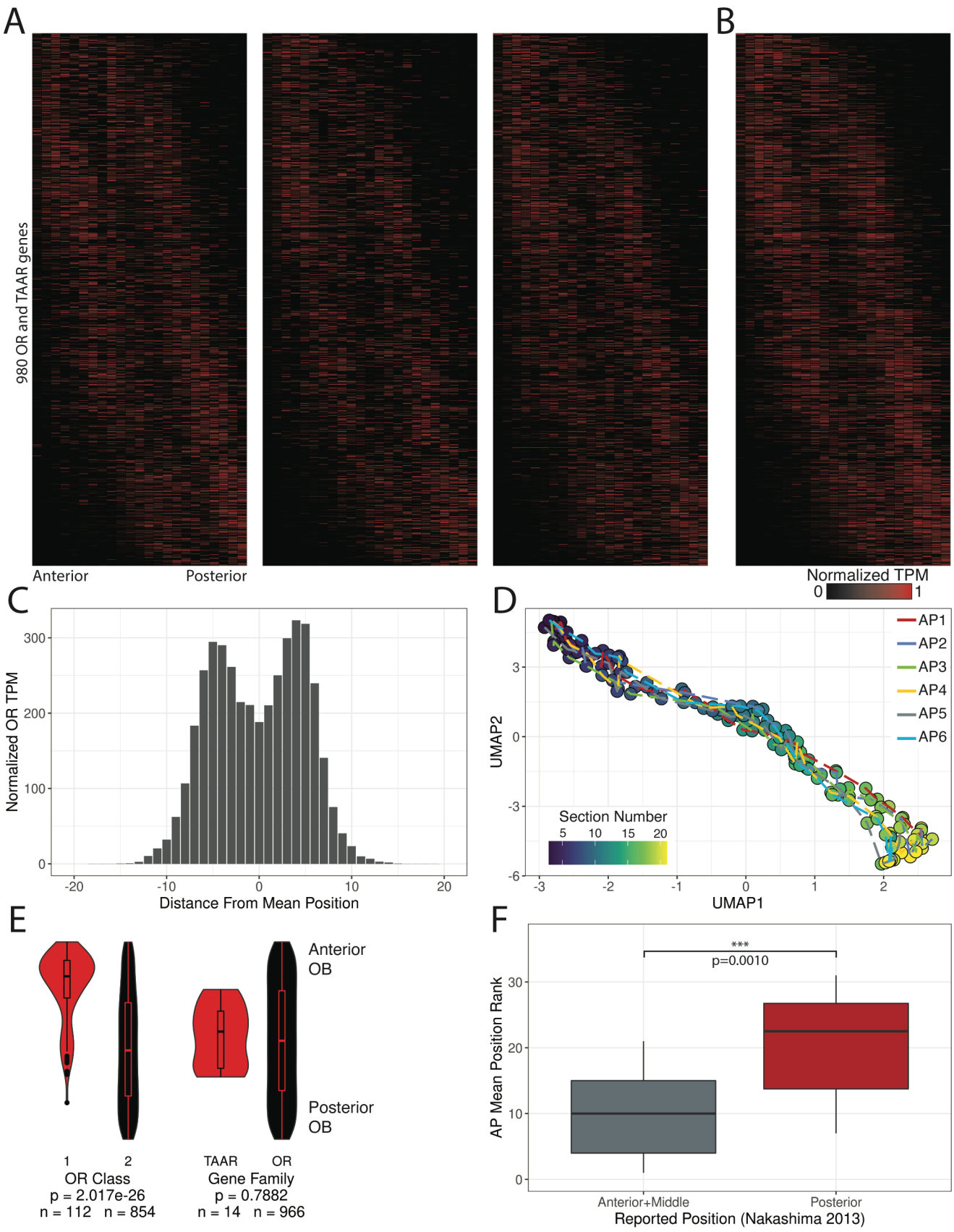

Fig. 3. Glomerular OR expression is bimodally distributed along the anteroposterior

axis. (**A**) Heatmaps for 980 ORs and TAARs across 23 AP sections sorted by mean position of expression from three replicate mice. (**B**) Merged representation from A. Ordering of genes is consistent across all heatmaps. (**C**) Distribution of normalized TPM (maximum observed value = 1, minimum observed value = 0) for all 980 ORs and TAARs from position of mean expression. (**D**) UMAP projection of 23 AP sections across all six replicates. (**E**) Distribution of ranked AP mean positions for the 980 ORs and TAARs by OR class and gene family. Statistic is Mann-Whitney U-test. (**F**) Distribution of the ranked AP mean position for the set of ORs cloned from the anterior and middle OB positions vs the posterior OB position from Nakashima et al. *Cell*. 2013. Statistic is Mann-Whitney U-test.

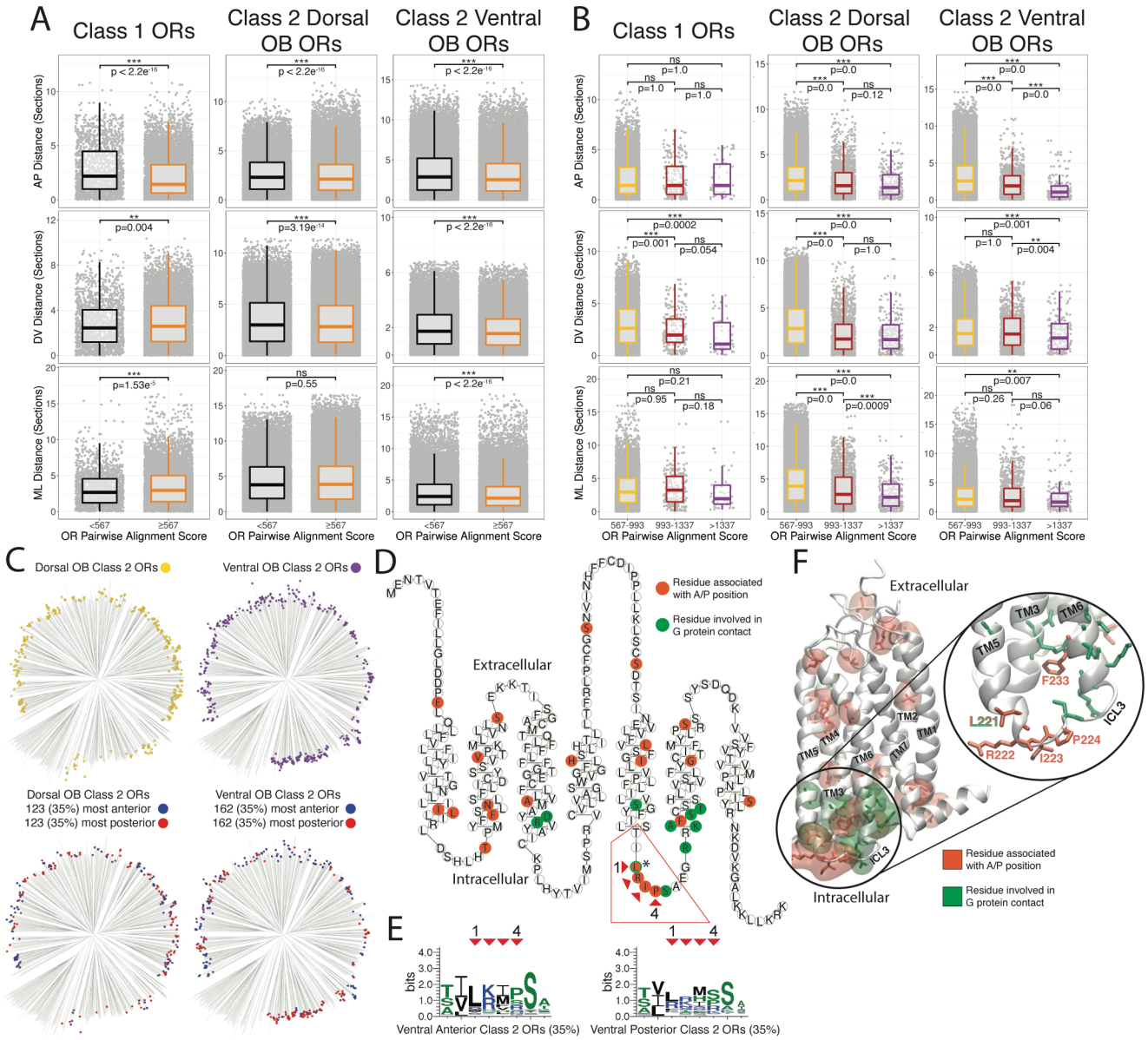

Fig. 4. OR sequence similarity correlates with glomerular position more strongly among ventral than dorsal Class II ORs. (**A**) Pairwise comparisons between mean position distance and OR protein alignment score for all ORs separated by an alignment score cutoff relating to OR percent identity for family level classification with ORs below the family level score cutoff (<567) in black and above the family level score cutoff (≥567) in orange for the AP (top), DV (middle), and ML dimensions (bottom). Statistic is Mann-Whitney U-test. For Class I, n in "<567" = 1778, n in "≥567" = 8934. For Class II dorsal ORs, n in "<567" = 19346, n in "≥567" = 87256. For Class II ventral ORs, n in "<567" = 26718, n in "≥567" = 37544. (**B**)

Pairwise comparisons between mean position distance and OR protein alignment score for ORs above family level classification (40%, 567) separated by an alignment score cutoffs relating to OR percent identity for subfamily level classification (60%, 993) and highly similar ORs (80%, 1337) for the AP (top), DV (middle), and ML dimensions (bottom). ORs falling within the range of family to subfamily level ORs (567-993) are displayed in yellow, subfamily to highly similar level ORs (993-1337) are displayed in red, and above the highly similar level OR score cutoff (>1337) in magenta. Statistic is Mann-Whitney U-test. For Class I, n in "567-993" = 8632, n in "993-1337" = 248, n in ">1337" = 54. For Class II dorsal ORs, n in "567-993" = 85144, n in "993-1337" = 1830, n in ">1337" = 282. For Class II ventral ORs, n in "567-993" = 36204, n in "993-1337" = 1126, n in ">1337" = 214. (**C**) Phylogenetic tree of all Class II dorsal OB ORs (top left, n = 354), all Class II ventral OB ORs (top right, n = 464), the most anterior (35%, blue) and most posterior (35%, red) Class II ORs from the dorsal (bottom left) and ventral OB (bottom right) DV zones. (**D**) Snakeplot of the Class II OR consensus protein sequence; orange residues have significantly different physicochemical properties for ventral, anterior or posterior, Class II ORs compared to all ventral Class II ORs. Green residues indicate residues known to be involved in Class A GPCR activation through contact with the G protein (* indicates the single residue which was identified as being both associated with G protein contact and identified as significantly different for ventral, anterior, Class II ORs). (**E**) Protein sequence logos for the four identified intracellular loop 3 residues associated with ventral Class II anterior/posterior ORs depicting the conservation of specific amino acid residues at each position. Red arrows indicate the specific residue within the Class II OR consensus snakeplot (C) and the corresponding position in the sequence logo. (**F**) Homology model of the mouse Class II consensus OR. Transmembrane helices (TM) are numbered with residues associated with A/P positions (orange) and residues in contact with the G protein (green) depicted in licorice with transparent regions indicating the residue surface. Right,

751 highlight of intracellular loop 3 (ICL3) where residues associated with A/P positions are

752 intermingled with the residues in contact with the G protein.

753

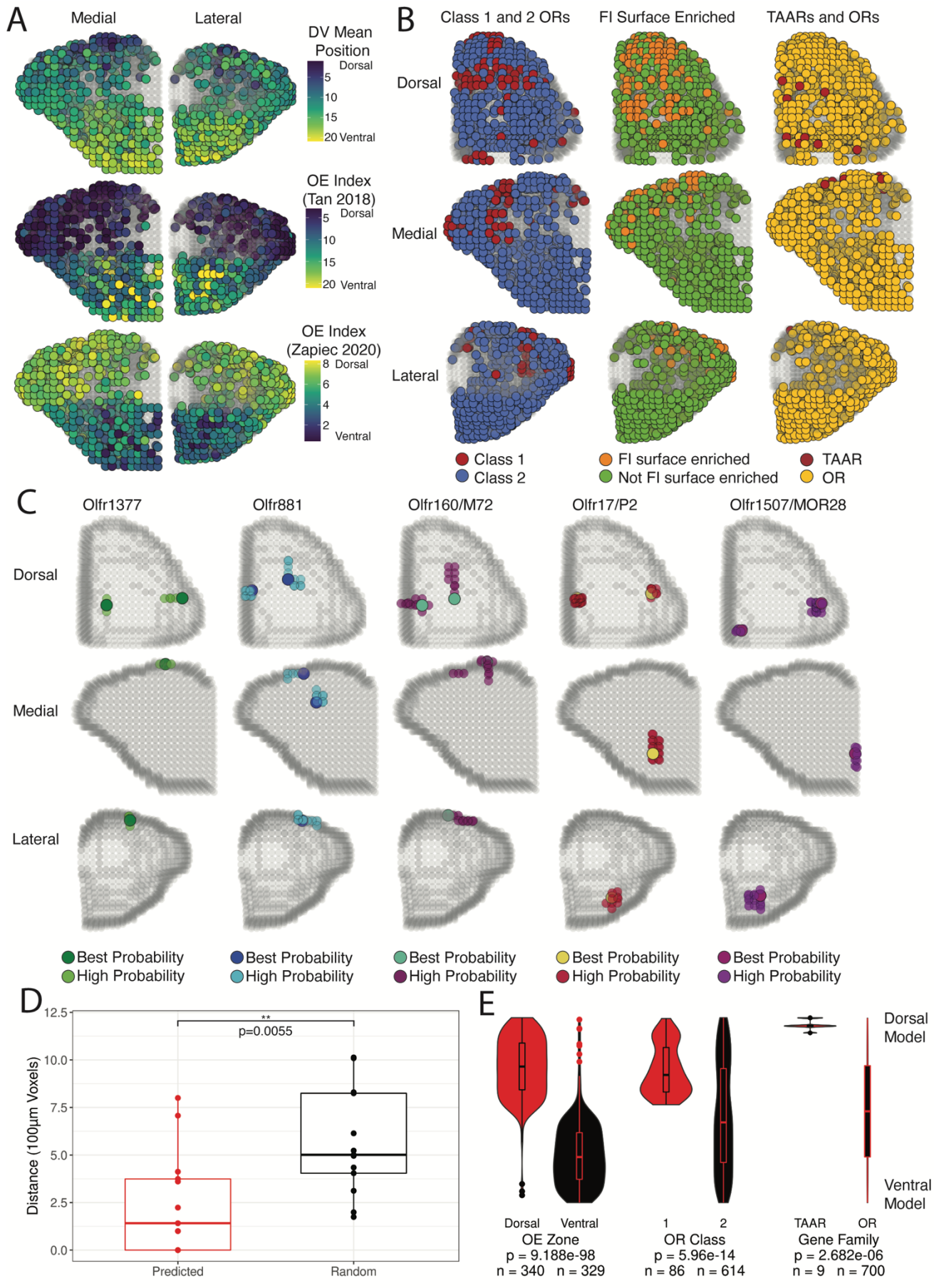

754

Fig. 5. A three-dimensional model for OR glomerular positions from combined single-dimension targeted sequencing data. (**A**) Three-dimensional predictions for the 709 ORs and TAARs with DV mean positions (top) and with observed values in OE DV indices (middle and bottom). (**B**) Three-dimensional predictions for the 709 ORs and TAARs with colors revealing contrasting distributions of Class I vs Class II ORs, functional imaging surface enriched vs not enriched ORs, and TAARs vs ORs. (**C**) Three-dimensional predictions for labeled ORs generated in this study and from Zapiec and Mombaerts *PNAS* 2015. High probability positions indicate the set of adjacent voxels containing highly ranked probabilities for that OR with the best probability color indicates the voxel with the highest ranked probability within that cluster of voxels. (**D**) Distance between predicted OR position and OR positions determined from gene-targeted mouse lines compared to 50 random ORs from the same DV zone (15 ORs used for unusual zone) and side of the OB. Statistic is Mann-Whitney U-test. (**E**) Distribution of ranked mean DV model position for the best probability voxel in each predicted glomerulus for all 709 ORs and TAARs for OE zone, OR Class, and gene family. Statistic is Mann-Whitney U-test.

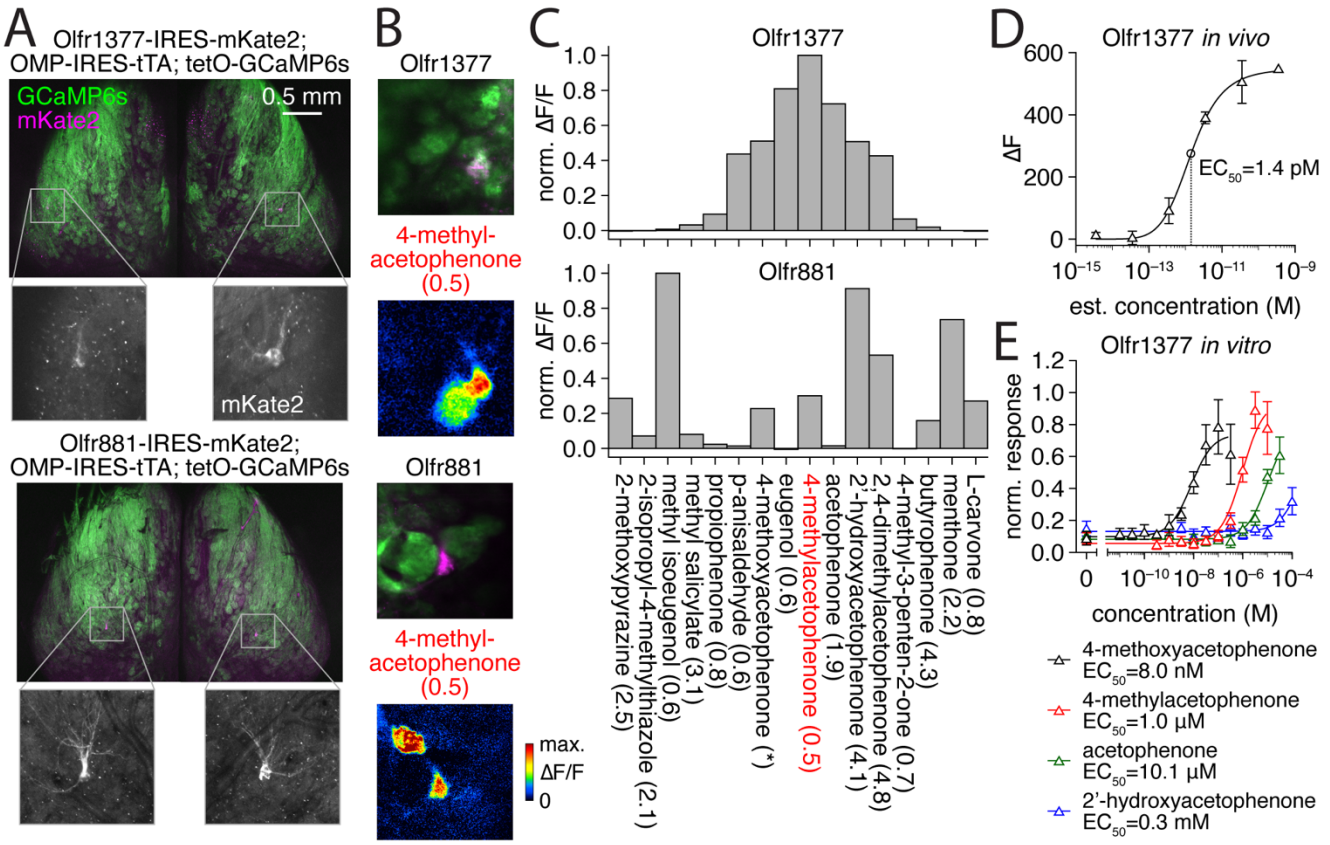

Fig. 6. Deorphanization of Olfr1377 and Olfr881. (**A**) Whole-mount confocal maximal intensity projection of compound heterozygous Olfr1377-IRES-mKate2; OMP-IRES-tTA; tetO-GCaMP6s and Olfr881-IRES-mKate2; OMP-IRES-tTA; tetO-GCaMP6s mice following two-photon functional imaging. (**B**) Baseline fluorescence and GCaMP6s ΔF/F responses to 2-s presentation of 4-methylacetophenone during two-photon functional imaging of the heterozygous lines in (A). Estimated concentration of delivered odorant (in nM) provided in parentheses here and elsewhere. Olfr1377 response map scaled from 0-80% ΔF/F. Olfr881 response map scaled from 0-30% ΔF/F. (**C**) Spectra of Olfr1377 and Olfr881 glomerular ΔF/F responses (sorted by Olfr1377 response magnitude) to a subset of ligands detected within a larger odorant panel. Odorants presented at an estimated concentration on the order of 10^0 nM, with the exception of 4-methoxyacetophenone (~3.5 nM for Olfr881; ~3.5 x 10^{-3} nM for Olfr1377). (**D**) In vivo concentration-response function of the Olfr1377 glomerulus to 4-

783 methoxyacetophenone. (**E**) In vitro concentration-response function of the Olfr1377 receptor

784 to an array of cyclic ketone odorants.